Ⓔ

The January 2019 (M_w 6.7) Coquimbo Earthquake: Insights from a Seismic Sequence within the Nazca Plate

by Sergio Ruiz, Jean-Baptiste Ammirati, Felipe Leyton, Leoncio Cabrera, Bertrand Potin, and Raúl Madariaga

ABSTRACT

On 20 January 2019, the Chilean cities of Coquimbo and La Serena were shaken by an intraplate earthquake of M_w 6.7 located at 70 km depth. High peak ground acceleration values and macroseismic intensities were reported. The mainshock was followed by more than 150 aftershocks higher than M_L 2.5, a seismic sequence completely recorded by local stations. Using a 3D velocity model, we precisely located the seismicity. The aftershocks were located some 20 km above and shifted from the mainshock but still inside the Nazca plate. We also performed moment tensor inversion of nine events obtaining mostly normal-fault focal mechanisms and kinematic inversions using the elliptical-patch approach. We found that the mainshock broke an approximated zone of 6 km by 8 km, propagated upward in the northwest direction and away from the aftershock area. The rupture inverted from accelerograms containing up to 1 Hz was characterized with a high stress drop of 7.51 MPa and a short seismic source time function of only 3 s duration.

Supplemental Content: Tables and figures describing some characteristics of the M_w 6.7 Coquimbo earthquake and the Chilean subduction zone.

INTRODUCTION

Chilean intraplate intermediate depth events are more frequent than the observed rate of 20% of the total earthquakes reported worldwide (Frohlich, 2006). During 2018, more than half of the Chilean seismicity was located deeper than 60 km. Since the twentieth century, several destructive intraplate earthquakes have occurred along the Chilean subduction: Chillán 1939 (M_w 7.8), Calama 1950 (M_w 8.2), Punitaqui 1997 (M_w 7.1), and Tarapacá 2005 (M_w 7.8) (Kausel and Campos, 1992; Beck *et al.*, 1998; Peyrat *et al.*, 2006; Delouis and Legrand, 2007; Ruiz and Madariaga, 2018). Among these, the most destructive was the Chillán 1939

earthquake, with a death toll of ~20,000 (Ruiz and Madariaga, 2018). On 20 January 2019 at 01:32:50 UTC, an earthquake of magnitude M_w 6.7 struck La Serena and Coquimbo, two densely populated cities on the Chilean coast (Fig. 1). The modified Mercalli macroseismic intensities reported by Chilean emergency agency reached VIII in those cities (Ⓔ Table S1, available in the supplemental content to this article); meanwhile the largest horizontal peak ground acceleration (PGA) was 0.56g, one of the highest PGA recorded in Chile to date (Idini *et al.*, 2017). This event occurred in north central Chile, a very active seismic zone, where the last megathrust event took place in 1730; more recently, the Punitaqui 1997 earthquake (M_w 7.1), a slab-push earthquake, and the subduction interplate events of Tongoy 2013 (M_w 6.6) and Illapel 2015 (M_w 8.3) earthquakes occurred (Fig. 1; Lemoine *et al.*, 2001; Ruiz and Madariaga, 2018).

The rupture mechanism of intraplate events is not completely understood, and several models attempt to explain this process (i.e. Prieto *et al.*, 2012; Poli *et al.*, 2016; Ferrand *et al.*, 2017). Moreover, several observations have shown that the Nazca plate exhibits a double seismic zone, well documented in northern and central Chile (Comte and Suaréz, 1994; Marot *et al.*, 2013; Sippl *et al.*, 2018). Results from Ruiz and Madariaga (2011) show that an M_w 6.7 earthquake, the 2007 Michilla event, occurred in the upper plane of the Nazca plate (Pastén-Araya *et al.*, 2018), whereas others have broken a larger zone of the oceanic plate, such as Tarapacá 2005, M_w 7.7 (Peyrat *et al.*, 2006; Deluois and Legrand, 2007).

Here, we use data recorded by the dense network managed by the National Seismological Center (CSN) of the University of Chile (Fig. 1) to study the 2019 Coquimbo intraplate seismic sequence. We were able to precisely relocate aftershocks and compute the moment tensor of the mainshock along with other larger magnitude aftershocks. In addition, we perform kinematic inversions to get a better understanding of the mainshock rupture process. Two datasets were used for inversion,
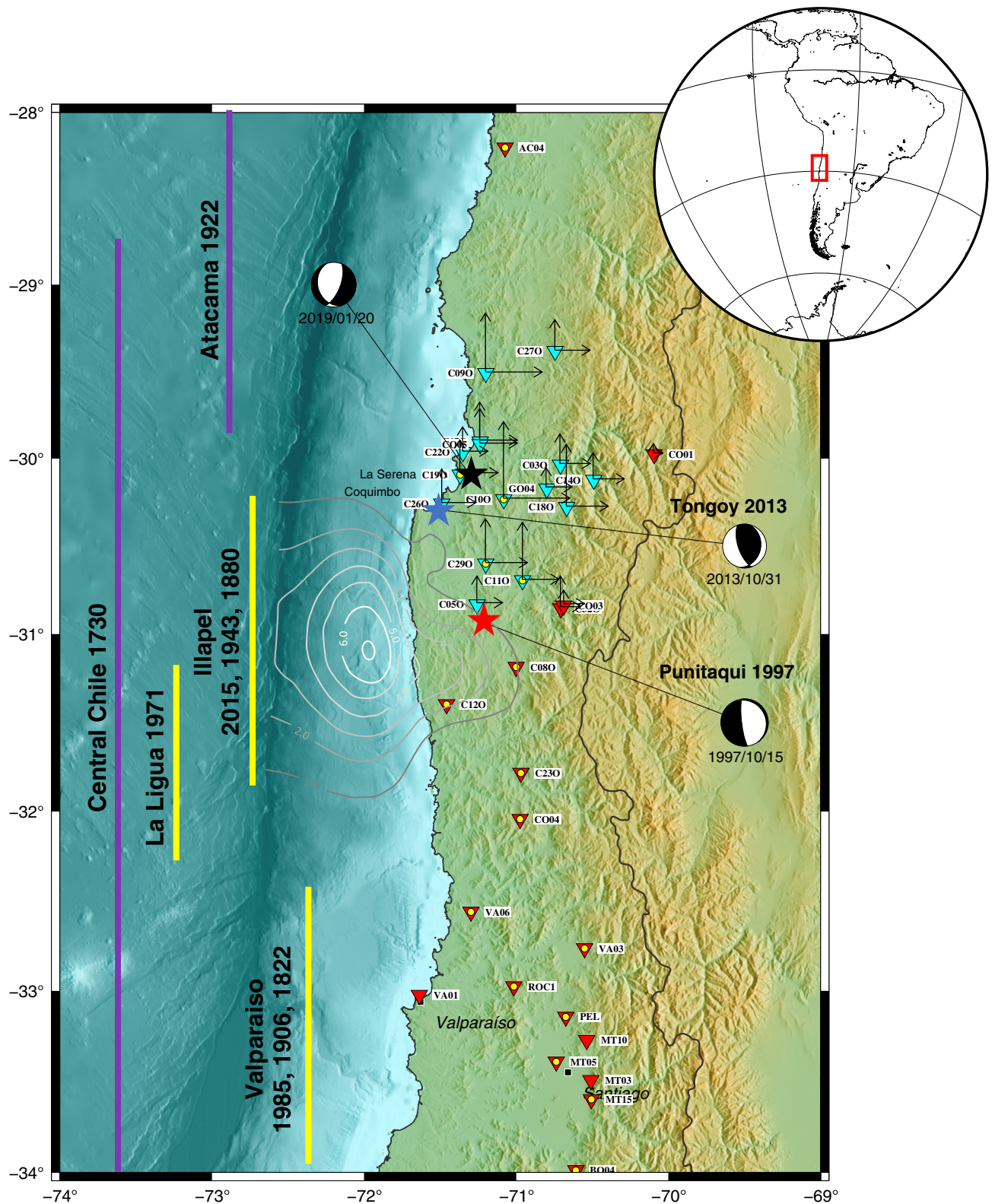
▲ **Figure 1.** Seismological context of north central Chile. Vertical lines represent the rupture length of major interplate earthquakes. Lines correspond to giant megathrust and recent earthquakes (Ruiz and Madariaga, 2018). Iso-contours correspond to the slip in meters of Illapel rupture zone (Ruiz et al., 2016). Stars denote the epicenter of the Coquimbo 2019, Punitaqui 1997, and Tongoy 2013 earthquakes. Cyan inverted triangles mark the local strong-motion stations, red inverted triangles correspond to regional strong-motion stations, and dotted triangles are stations used in the section record of Figure 2. Vectors on stations are north and east peak ground acceleration, with the largest being 0.56g at station C10O. (Inset) Global map with the specified study area. The color version of this figure is available only in the electronic edition.
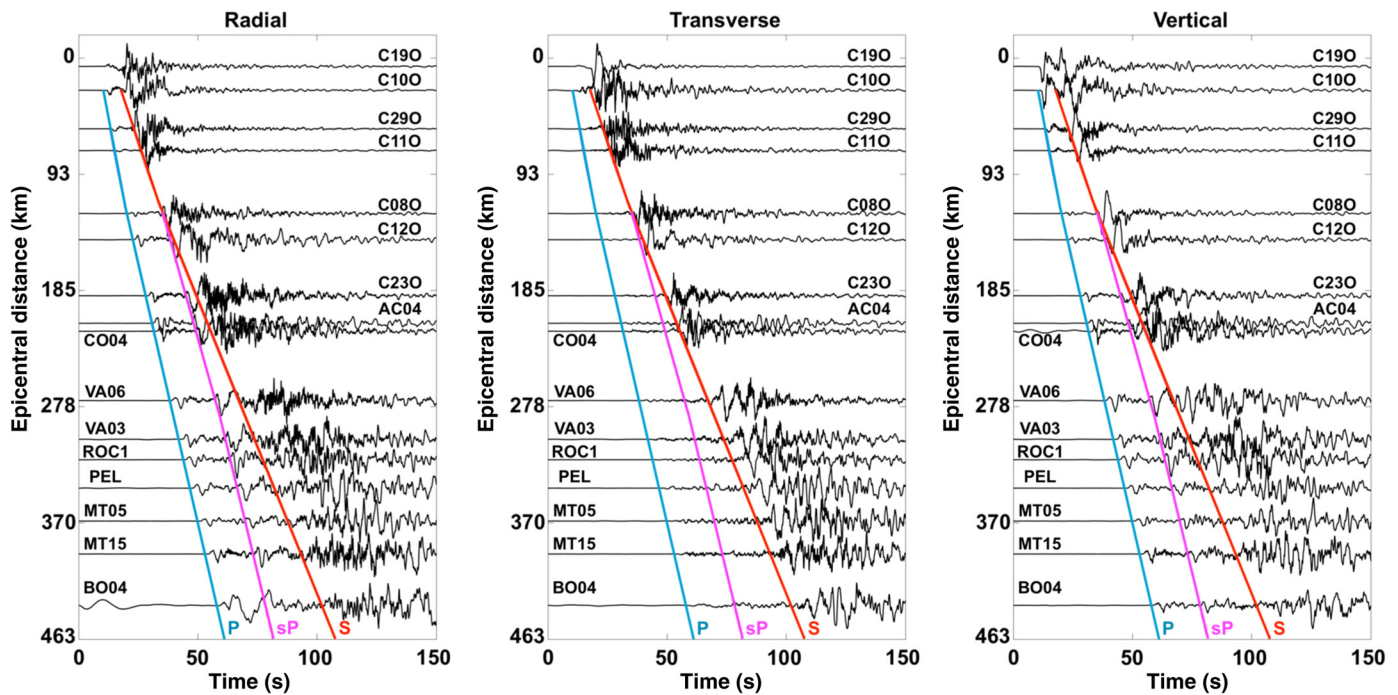
▲ **Figure 2.** Displacement record section for stations indicated in Figure 1. The horizontal components (east–west and north–south traces) were rotated into radial and transverse components. The *sP* wave is clear in the radial and vertical components, but in the transverse component, only the *S* wave is clearly observed along with the surface waves. The color version of this figure is available only in the electronic edition.

one of regional stations and another that includes only the stations close to the mainshock epicenter. From these analyses, we discuss the observed short source time function of 3 s, with a rupture propagating in the northwest direction, away from the aftershock sequence. We also discuss the mantle densification process that could have controlled the mainshock nucleation, around the 600°C isotherm, while the aftershocks clustered along two parallel planes around 450°C.

DATA AND METHODOLOGY

Data and Coquimbo Seismic Sequence

Nineteen CSN strong-motion instruments recorded the mainshock at epicentral distances shorter than 125 km. Some of these stations record in continuous time; others use a trigger system. These stations are three-component EpiSensor accelerometers with 200 samples per second. In addition, broadband stations from the permanent CSN network are available in this area, mostly Trillium of 120 s and two stations with STS2 (GO04 and PEL), as shown in Figures 1 and 2. We use these data to analyze the 153 events reported by the CSN from 20 to 28 January 2019 and the eight largest magnitude aftershocks ($M_w > 4.0$) reported up to 39 days after the mainshock.

In Figure 2, we show a record section of strong-motion data from the mainshock; they were doubly integrated to displacement using a high-pass Butterworth filter of corner frequency 0.05 Hz. This filter enables the visualization of *P* and *S* waves in the local records, and the *P*, *sP*, *S*, and surface waves

from the regional stations. In local station records, both *P* and *S* direct body waves exhibit durations shorter than 3 s. More distant stations show a larger duration for *P* and *S* waves because of the simultaneous arrival of refracted and reflected *P* and *S* waves as well as *sP* waves. This is the reason why, at farther stations, the seismograms are controlled by *sP* and surface wave in contrast to the closest stations, mainly controlled by direct body waves. Hence, we decided to build two databases to perform our kinematic inversions: one considering only local stations (hypocentral distance <100 km) and another using regional stations (hypocentral distance >100 km).

Localization and Moment Tensor

We use local and regional strong-motion and broadband data to relocate 153 events detected by the CSN during a period of eight days after the mainshock; we also included the aftershocks of magnitude larger than M_w 4.0 that occurred during an extended period of 39 days (from the CSN database; see Data and Resources). We consider a 3D velocity model, previously built by inverting more than 150,000 *P* and *S* arrivals from the CSN database for the 2000–2018 period, using a Bayesian approach (Potin, 2016). Probabilistic locations are obtained using the NonLinLoc code (Lomax *et al.*, 2000). For each hypocenter location, we consider a minimum of eight phases (*P* or *S*) including at least two *S* phases. Then we apply a double-difference technique to obtain the relative localization of the aftershocks (Waldhauser and Schaff, 2008).

Finally, we select events with magnitudes larger than 4 presenting high signal-to-noise ratio and compute the full moment tensor using the ISOLated Asperities (ISOLA) code (Sokos and Zaharadnik, 2008; Vackář et al., 2017). We obtain moment tensors for nine events for which we minimized the variance between observed and synthetic waveforms. The data were filtered using a band-pass filter of corner frequencies 0.1–0.2 Hz for traces recorded by local stations and 0.01–0.1 Hz for regional waveforms. A representative 1D velocity model for the Chilean subduction margin was used for both moment tensor and kinematic inversions (Ⓔ Table S2).

Regional and Local Finite-Fault Model Using An Elliptical-Patch Approach

In the present study, we assume a finite-fault model with an *a priori* elliptical-patch distribution. This strategy has been successfully used by several authors: Vallée and Bouchon (2004), Ruiz and Madariaga (2011, 2013), Twardzik et al. (2014), Ulrich and Aochi (2015), Herrera et al. (2017), Mirwald et al. (2019), Momeni et al. (2019), among others. To invert for the slip distribution of the mainshock, we propose a two-step approach. First, we performed a kinematic inversion considering only regional data mostly characterized by long-period waveforms (Figs. 1 and 2), obtaining 10 parameters. We applied this first step to identify the most probable rupture plane, which is inverted during this regional inversion (Leyton et al., 2018). Then we performed a second kinematic inversion considering only seven parameters, fixing the rupture plane previously defined, and used a higher corner frequency to filter the data recorded by the local stations (Figs. 1 and 2).

Regional Elliptical-Patch Approach
As described previously, in a first step we considered only regional strong-motion records. We corrected for the instrument response and linear trend of each trace and filtered using a causal Butterworth filter with corner frequencies of 0.02 and 0.2 Hz. Finally, we integrated the traces into displacement. The seismograms used in the inversion were manually selected after visual inspection of all available records. We considered a time window of 20 s before the *P*-wave arrival and up to 180 s after the *S*-wave arrival, including in our inversion both body and surface waves. Finally, we inverted 10 parameters to characterize the focal mechanism, magnitude, and slip distribution of Coquimbo 2019 earthquake. Among these 10 parameters, five correspond to geometric parameters: the two semi-axes, the position of centroid, and azimuthal angle of ellipse; three correspond to rupture plane parameters: strike, dip, and rake; one parameter to define the rupture velocity; and one parameter to define the maximum amplitude of a Gaussian slip distribution inside of the elliptical rupture zone. We use a nonlinear inversion method based on a modified neighborhood algorithm (Leyton et al. 2018).

Local Elliptical-Patch Approach
We perform a second kinematic inversion using the same approach detailed previously; however, in this second step,

we use a rupture plane obtained previously to reduce the number of parameters. In this inversion, we considered only local data (Fig. 1) that have higher frequency content than regional station. The strong-motion records are handled following the same steps described previously, but here we filtered in a broader frequency band from 0.02 to 1 Hz. We evaluate the fit between real and synthetic records using an L2 norm starting from origin time up to 40 s later to avoid including surface waves. In this case, we use a crack-type rupture considering an elliptical contour instead of a Gaussian distribution as we used in the regional data inversion. From the inverted rupture model, we can compute dynamic parameters using a circular crack approximation obtained by averaging both axes of the ellipse (Madariaga and Ruiz, 2016; Ruiz et al., 2017).

RESULTS

Hypocenter Localization and Moment Tensor Results
Using our 3D velocity model, our results for the mainshock indicate a hypocenter at 71.38° W, 30.10° S, and 72 km depth, with an origin time of 01:32:51.20 UTC. These results are consistent with the hypocenter reported by the CSN (71.3° W, 30.1° S, 70 km depth, at 01:32:50 UTC) using a 1D velocity model. These hypocenters appear shifted only by few kilometers from the revised U.S. Geological Survey solution (71.382° W, 30.040° S, 63 km). The mainshock hypocenter is located within the Nazca plate, ∼30 km below the top of the Nazca slab proposed by Hayes et al. (2018) (Fig. 3). Aftershocks show a distribution dipping to the southeast with depths consistently shallower than the mainshock, located ∼15 km below the top of the slab. We do not observe any particular temporal or spatial relationship among the aftershocks. The focal mechanism associated with the mainshock corresponds to a normal slab-pull (tensional) rupture with focal plane dip angles of 66° and 33°, respectively. The focal mechanisms for the larger magnitude aftershocks (in blue) appear to be similar to the mainshock. The pink and yellow focal mechanisms are interplate events that also occurred after the mainshock; see Figure 3. The double-difference relocation of aftershocks shows a cluster along two parallel planes separated by 5–10 km (Fig. 3).

Kinematic Inversion of Finite-Fault Model Elliptical-Patch Approach Using Regional and Local Data
Regional Elliptical-Approach Inversion
Our preferred solution presents northwest rupture propagation from the hypocenter. The elliptical rupture ellipse is 30 km by 25 km, and the Gaussian slip distribution indicates a maximum slip of 0.71 m. Our fault plane is 31° ± 18° strike, 66° ± 9° dip, and −72° ± 18° rake, which is very similar to one of the nodal planes obtained from moment tensor inversion (21° strike, 66° dip, and −72° rake). The other parameters are rupture velocity of 2.7 km/s and a seismic moment of 1.43×10^{19} N · m equivalent to moment magnitude of 6.7, which is slightly higher than the seismic moment that we obtained from seismic moment tensor (Ⓔ Table S3). Ⓔ Figure S1a shows the
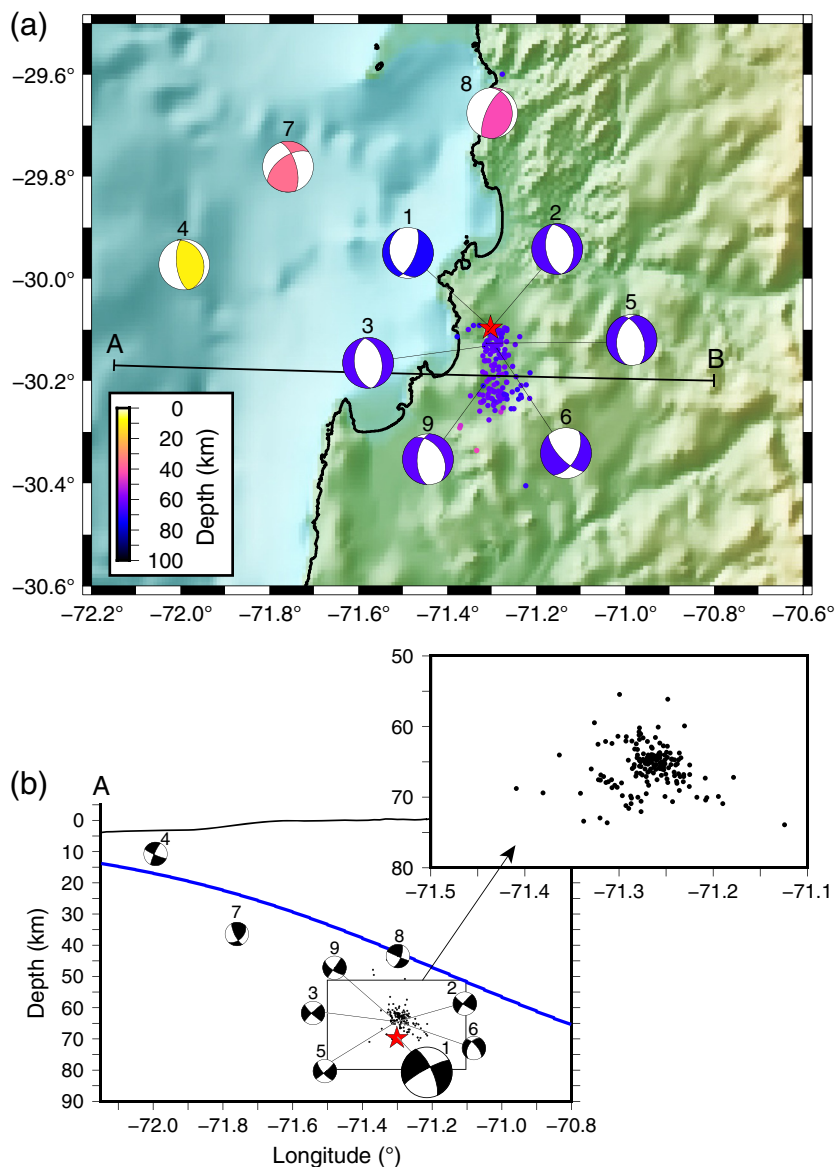
▲ **Figure 3.** (a) Epicentral distribution of the mainshock (star) and aftershock sequence (dots). Focal mechanisms for the mainshock and some aftershocks (see main text) are shown with compressive quadrants colored according to focal depth. (b) Cross section along segment AB in (a). The event numbers 4, 7, and 8 are probably part of the background seismicity, located at the plate interface. The slab line corresponds to the projection along AB of the Nazca slab model SLAB2 (Hayes et al., 2018). The zoomed section shows the double-difference relocation of the aftershock sequence. Focal mechanism numbers refer to focal mechanism solutions in Ⓔ Table S3. The color version of this figure is available only in the electronic edition.

obtained slip distribution, and Ⓔ Figure S1b shows the comparison between observed and synthetic waveforms.

Local Elliptical-Approach Inversion
In this case, we consider a fixed plane (21° strike, 66° dip, and −72° rake), which is the fault plane obtained from moment tensor inversion that is similar to the solution obtained from our regional kinematic inversion. The rupture area estimated using

local data is much smaller than the regional inversion with lengths of semi-axis of 5.94 and 7.81 km. The rupture propagated in the northwest direction with a rupture velocity of 2.87 km/s, slightly faster than that obtained from regional inversion. The rest of parameters are shown in Ⓔ Table S4. Figures 4 and 5 show the elliptical slip distribution contours along with the agreement between observed and synthetic data for each local station. The average semi-axis is 6.9 km long; then considering a circular crack model rupture (equation 1), we obtain a stress drop of 7.51 MPa, which is similar to the values usually observed for intraplate earthquakes.

$$\Delta\sigma = \frac{7}{16}\frac{M_0}{a^3} \tag{1}$$

DISCUSSION

Duration of the Seismic Source
Local strong-motion records show clear P and S direct waves characterized by a short duration of only 3 s (Figs. 2 and 4); this short duration is consistent with the stress drop calculated from our slip distribution inversion. The short duration observed in this work contrasts with the duration of other events of similar magnitude around the world (Chounet and Vallée, 2018). For example, here we make a brief comparison with some similar magnitude events: Tongoy 2013 M_w 6.6 and Puebla 2017 M_w 7.1, which have longer seismic source duration. We also look at the Michilla 2007 M_w 6.7 earthquake, which also has short seismic source duration.

The 31 October 2013 Tongoy earthquake was an event of magnitude M_w 6.6 that occurred in the same area at the interplate contact, near the bottom of the seismogenic zone (see Fig. 1). The stack of seismograms recorded in North America show a duration of >10 s in comparison with the 3 s observed during the Coquimbo earthquake (Ⓔ Fig. S2). Recently, the rupture process of the 2017 Puebla intraplate earthquake (M_w 7.1) in Mexico has been identified as slow and energetically inefficient (Mirwald et al., 2019). With a hypocentral depth of 57 km, the 2017 Puebla earthquake is shallower than the 2019 Coquimbo earthquake; even though both present similar stress-drop values, the rupture duration is more than five times longer for the 2017 Puebla earthquake compared with the 2019 Coquimbo earthquake. Finally, on 12 December 2007, the Michilla intraplate event of magnitude M_w 6.7 occurred in northern Chile. Its
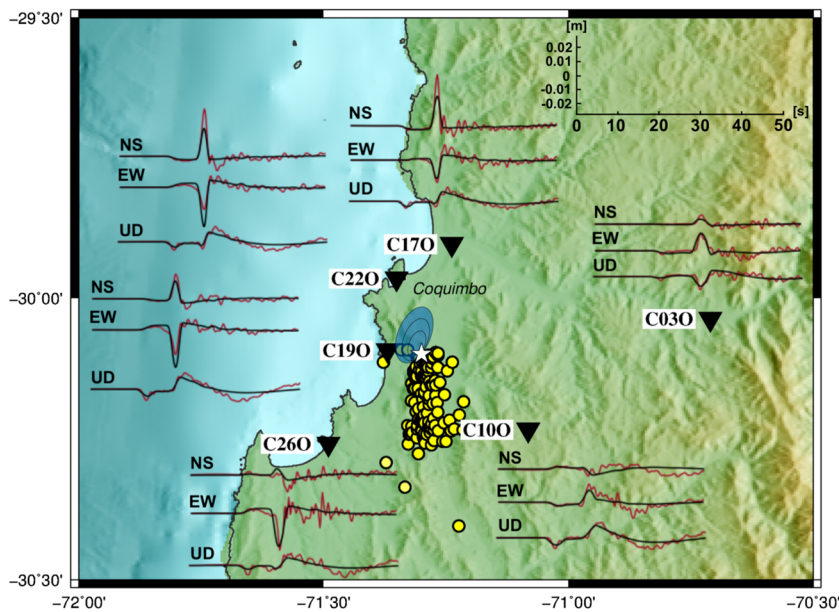
▲ **Figure 4.** Ellipse shows the rupture area of the mainshock, with at maximum slip amplitude of 0.72 m. Lines within the elliptical slip area are 1 s isochrones. The white star is the National Seismological Center (CSN) mainshock epicenter, and the yellow dots show the aftershock distribution. Simulated (black) and real (brown) traces are shown, next to each station. NS, north–south; EW, east–west; UD, up–down. The color version of this figure is available only in the electronic edition.

hypocenter was estimated at 43 km depth, within the oceanic crust at the top of the Nazca plate; see Ⓔ Figure S3 (Ruiz and Madariaga, 2011; Pastén-Araya *et al.*, 2018). The seismic rupture of the 2007 earthquake had a rupture duration shorter than 5 s, with a stress drop quite similar to the 2019 Coquimbo event.

2007 Michilla and 2019 Coquimbo: Earthquakes Located within the Nazca Plate

Both the 2007 Michilla and the 2019 Coquimbo earthquakes occurred inside of the Nazca plate: the first is located in the oceanic crust near the top of the Nazca plate, and the 2019 Coquimbo earthquake is located in the lower plane of the double seismic zone reported in some close profiles by Marot *et al.* (2013). As mentioned, both earthquakes present similar seismic rupture characteristics. However, we would have expected differences in the rupture process due to differences in pressure and temperature (PT) conditions (Frohlich, 2006). In Figure 5, we schematically show the position inside of the Nazca plate of the Coquimbo 2019 mainshock hypocenter and its direction of propagation, along with the aftershocks and the slab 2.0 (Hayes *et al.*, 2018). We add isotherms using a simplified approach based in the distance to the trench and age of the Nazca plate in this zone assuming the cooling of a semi-infinite half-space model (Turcotte and Schubert, 1982):

$$z = erf^{-1}\left(\frac{T - T_0}{T_m - T_0}\right) 2\sqrt{\kappa t}, \qquad (2)$$

in which z and T are the depth and the temperature of the isotherm, respectively; T_0 is the surface temperature (0°C); T_m is the temperature beneath the plate (1300°C); κ is thermal diffusivity (8×10^{-7} m^2/s); and t is the plate age (40 Ma).

The mainshock is located at 600°C, and the aftershocks are clustered along two parallel planes around 450°C. Some studies (e.g., Duesterhoeft *et al.*, 2014) demonstrated that the densification of the subducting ocean mantle by metamorphic reactions could contribute to the slab pull, especially when this phenomenon occurs close to the trench, where PT conditions do not allow the eclogitization of the subducting oceanic crust. The Coquimbo 2019 earthquake occurred at ~70 km, deep within the slab but only ~120 away from the trench and thus could be a good example of seismicity associated with mantle densification. In contrast, the 2007 Michilla earthquake probably had a brittle rupture associated to older outer-rise bending faults, so the most plausible reason for the earthquake trigger mechanism is a consequence of the reduction of effective normal stress induced by increased pore pressure during dehydration reactions (Ranero *et al.*, 2003; Pastén-Araya *et al.*, 2018).

Spatial Distribution of Mainshock and Aftershocks of Intraplate Events

Another interesting feature that we observe in the Coquimbo aftershocks is somewhat similar to that of the Anchorage, Alaska, 2018 intraplate earthquake (Liu *et al.*, 2019). This intraslab earthquake of magnitude 7.1 occurred inside the underthrusted Pacific plate at depths from 45 to 65 km and had an aftershock sequence located shallower than the slip distribution. Why do the aftershocks distributions observed in Coquimbo 2019 and Anchorage 2018 not follow the same pattern as interplate seismicity? These observations show that the aftershocks are not located at the boundaries of the mainshock slip distribution as often observed for shallow and interplate events (Wetzler *et al.*, 2018).

CONCLUSIONS

The Coquimbo 2019 slab-pull earthquake occurred in an active seismic zone. The hypocenter of the mainshock has been located at 70 km depth close to the 600°C isotherm within the Nazca slab. The aftershocks were located in a shallower zone, around the 450°C isotherm. The accelerograms of the mainshock are clearly dominated by P and S direct waves, which have duration of only 3 s. This short duration could be determined because of the dense accelerometer network available in the Coquimbo region. The duration agrees with a rupture characterized by a radius smaller than 7 km. The stress drop
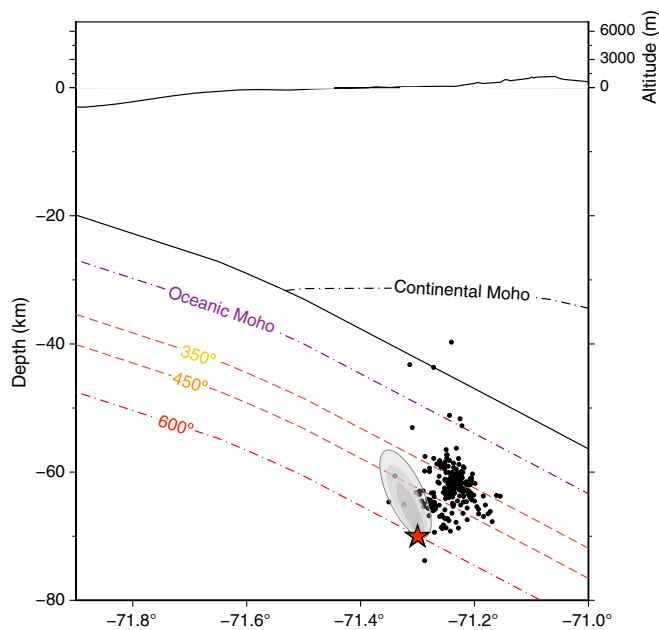
▲ **Figure 5.** Schematic profile of the Nazca plate and the hypo-central localizations. The segmented lines correspond to the isotherms. The red star is the hypocenter of the mainshock; black dots are the position of aftershocks relocated using double difference. The ellipse is the slip distribution obtained from local data; the gray scale changes each second during the rupture process. For reference, we added the continental Moho proposed by Tassara and Echaurren (2012). The color version of this figure is available only in the electronic edition.

of this rupture zone was 7.51 MPa, similar to other intraplate earthquakes located at different isotherms within the subduction zone. However, the aftershocks are not located along the same plane of the as mainshock. This was also observed for the Anchorage 2018 earthquake (Liu *et al.*, 2019), a feature that could be common for intraplate earthquakes that start at the bottom of the plate.

DATA AND RESOURCES

ACKNOWLEDGMENTS

REFERENCES

Beck, S., S. Barrientos, E. Kausel, and M. Reyes (1998). Source characteristics of historic earthquakes along the central Chile subduction zone, *J. S. Am. Earth Sci.* **11,** 115–129.

Chounet, A., and M. Vallée (2018). Global and interregion characterization of subduction interface earthquakes derived from source time functions properties, *J. Geophys. Res.* **123,** no. 7, 5831–5852.

Comte, D., and G. Suárez (1994). An inverted double seismic zone in Chile: Evidence of phase transformation in the subducted slab, *Science* **263,** no. 5144, 212–215, doi: 10.1126/science.263 .5144.212.

Delouis, B., and D. Legrand (2007). M_{w} 7.8 Tarapacá intermediate depth earthquake of 13 June 2005 (northern Chile): Fault plane identification and slip distribution by waveform inversion, *Geophys. Res. Lett.* **34,** no. 1, doi: 10.1029/2006GL028193.

Duesterhoeft, E., J. Quinteros, R. Oberhänsli, R. Bousquet, and C. de Capitani (2014). Relative impact of mantle densification and eclogitization of slabs on subduction dynamics: A numerical thermodynamic/thermokinematic investigation of metamorphic density evolution, *Tectonophysics* **637,** 20–29. doi: 10.1016/ j.tecto.2014.09.009.

Ferrand, T. P., N. Hilairet, S. Incel, D. Deldicque, L. Labrousse, J. Gasc, J. Renner, Y. Wang, H. W. Green II, and A. Schubnel (2017). Dehydration-driven stress transfer triggers intermediate-depth earthquakes, *Nature Commun.* **8,** 15,247.

Frohlich, C. (2006). *Deep Earthquakes*, Cambridge University Press, Cambridge, United Kingdom.

Hayes, G. P., G. L. Moore, D. E. Portner, M. Hearne, H. Flamme, M. Furtney, and G. M. Smoczyk (2018). Slab2, a comprehensive subduction zone geometry model, *Science* **362,** no. 6410, 58–61.

Herrera, C., S. Ruiz, R. Madariaga, and P. Poli (2017). Dynamic inversion of the 2015 Jujuy earthquake and similarity with other intraslab events, *Geophys. J. Int.* **209,** no. 2, 866–875 doi: 10.1093/gji/ggx056.

Idini, B., F. Rojas, S. Ruiz, and C. Pastén (2017). Ground motion prediction equations for the Chilean subduction zone, *Bull. Earthq. Eng.*, doi: 10.1007/s10518-016-0050-1.

Kausel, E., and J. Campos (1992). The Ms = 8 tensional earthquake of 9 December 1950 of northern Chile and its relation to the seismic potential of the region, *Phys. Earth Planet. Int.* **72,** nos. 3/4, 220–235.

Lemoine, A., R. Madariaga, and J. Campos (2001). Evidence for earthquake interaction in Central Chile: The July 1997-September 1998 sequence, *Geophys. Res. Lett.* **28,** no. 14, 2743–2746.

Leyton, F., S. Ruiz, and R. Madariaga (2018). Focal mechanism, magnitude and finite fault rapid estimation using the elliptical patch method in Chile, *Seismol. Res. Lett.* doi: 10.1785/0220170174.

Liu, C., T. Lay, Z. Xie, and X. Xiong (2019). Intraslab deformation in the 30 November 2018 Anchorage, Alaska, M_{w} 7.1 earthquake, *Geophys. Res. Lett.* doi: 10.1029/2019GL082041.

Lomax, A., J. Virieux, P. Volant, and C. Berge (2000). Probabilistic earthquake location in 3D and layered models: Introduction of a Metropolis–Gibbs method and comparison with linear locations, in *Advances in Seismic Event Location*, C. H. Thurber and N. Rabinowitz (Editors), Kluwer, Amsterdam, The Netherlands, 101–134, doi: 10.1007/978-94-015-9536-0_5.

Madariaga, R., and S. Ruiz (2016). Earthquake dynamics on circular faults: A review 1970–2015, *J. Seismol.* **20,** 1235–1252, doi: 10.1007/s10950-016-9590-8.

Marot, M., T. Monfret, M. Pardo, G. Ranalli, and G. Nolet (2013). A double seismic zone in the subducting Juan Fernandez Ridge of the Nazca Plate (32°S), central Chile, *J. Geophys. Res.* **118,** no. 7, 3462–3475.

Mirwald, A., V. M. Cruz-Atienza, J. Díaz-Mojica, A. Iglesias, S. K. Singh, C. Villafuerte, and J. Tago (2019). The 19 September 2017 (Mw7.1), intermediate-depth Mexican earthquake: A slow and energetically inefficient deadly shock, *Geophys. Res. Lett.* **46**, doi: 10.1029/2018GL080904.

Momeni, S. M., A. Aoudia, M. Tatar, C. Twardzik, and R. Madariaga (2019). Kinematics of the 2012 Ahar–Varzaghan complex earthquake doublet (M_w 6.5 and M_w 6.3), *Geophys. J. Int.* **217,** no. 3, 2097–2124, doi: 10.1093/gji/ggz100.

Pastén-Araya, F., P. Salazar, S. Ruiz, E. Rivera, B. Potin, A. Makysmowicz, E. Torres, J. Villarroel, E. Cruz, J. Valenzuela, *et al.* (2018). Fluids along the plate interface influencing the frictional regime of the Chilean subduction zone, northern Chile, *Geophys. Res. Lett.*, doi: 10.1029/2018GL079283.

Peyrat, S., J. Campos, J. B. de Chabalier, A. Perez, S. Bonvalot, M.-P. Bouin, D. Legrand, A. Nercessian, O. Charade, G. Patau, E. Clévédé, *et al.* (2006). Tarapacá intermediate depth earthquake (Mw 7.7, 2005, northern Chile): A slab-pull event with horizontal fault plane constrained from seismologic and geodetic observations, *Geophys. Res. Lett.* **33,** no. 22, doi: 10.1029/2006GL027710.

Poli, P., G. Prieto, E. Rivera, and S. Ruiz (2016). Earthquakes nucleation and thermal shear instability in the Hindu-Kush intermediate-depth nest, *Geophys. Res. Lett.* **43,** 1537–1542, doi: 10.1002/2015GL067529.

Potin, B. (2016). Les AlpesOccidentales: Tomographie, localisation de séismesettopographie du Moho, *Ph.D. Thesis*, University Grenoble-Alpes (France), ISTerre (in French).

Prieto, G. A., G. C. Beroza, S. A. Barrett, G. A. López, and M. Florez (2012). Earthquake nests as natural laboratories for the study of intermediate-depth earthquake mechanics, *Tectonophysics* **570,** 42–56.

Ranero, C. R., J. P. Morgan, K. McIntosh, and C. Reichert (2003). Bending-related faulting and mantle serpentinization at the Middle America trench, *Nature* **425,** no. 6956, 367.

Ruiz, S., and R. Madariaga (2011). Determination of the friction law parameters of the Mw 6.7 Michilla earthquake in northern Chile by dynamic inversion, *Geophys. Res. Lett.* **38,** L09317, doi: 10.1029/2011GL047147.

Ruiz, S., and R. Madariaga (2013). Kinematic and dynamic Inversion of the 2008 northern Iwate earthquake, *Bull. Seismol. Soc. Am.* **103,** no. 2A, 694–708, doi: 10.1785/0120120056.

Ruiz, S., and R. Madariaga (2018). Historical and recent large megathrust earthquakes in Chile, *Tectonophysics*, doi: 10.1016/j.tecto.2018.01.015.

Ruiz, S., E. Klein, F. del Campo, E. Rivera, P. Poli, M. Metois, C. Vigny, J. C. Baez, G. Vargas, F. Leyton, R. Madariaga, and L. Fleitout (2016). The seismic sequence of the 16 September 2015 M_w 8.3 Illapel, Chile, earthquake, *Seismol. Res. Lett.* doi: 10.1785/0220150281.

Ruiz, S., H. Tavera, P. Poli, C. Herrera, C. Flores, E. Rivera, and R. Madariaga (2017). The deep Perú 2015 doublet earthquakes, *Earth Planet. Sci. Lett.* **478,** 102–109.

Sippl, C., B. Schurr, G. Asch, and J. Kummerow (2018). Seismicity structure of the Northern Chile forearc from >100,000 double-difference relocated hypocenters, *J. Geophys. Res.* **123,** no. 5, 4063–4087.

Sokos, E. N., and J. Zahradnik (2008). ISOLA a Fortran code and a Matlab GUI to perform multiple-point source inversion of seismic data, *Comput. Geosci.* **34,** no. 8, 967–977, doi: 10.1016/j.cageo.2007.07.005.

Tassara, A., and A. Echaurren (2012). Anatomy of the Andean subduction zone: Three-dimensional density model upgraded and compared against global-scale models, *Geophys. J. Int.* **189,** 161–168.

Turcotte, D., and G. Schubert (1982). *Geodynamics—Applications of Continuum Physics to Geological Problems*, John Wiley, Hoboken, New Jersey, 464 pp.

Twardzik, C., S. Das, and R. Madariaga (2014). Inversion for the physical parameters that control the source dynamics of the 2004 Parkfield earthquake, *J. Geophys. Res.* **119,** no. 9, 7010–7027.

Ulrich, T., and H. Aochi (2015). Rapidness and robustness of finite-source inversion of the 2011 Mw 9.0 Tohoku earthquake by an elliptical-patches method using continuous GPS and acceleration data, *Pure Appl. Geophys.* **172,** no. 12, 3439–3453.

Vackář, J., J. Burjánek, F. Gallovič, J. Zahradník, and J. Clinton (2017). Bayesian ISOLA: New tool for automated centroid moment tensor inversion, *Geophys. J. Int.* **210,** no. 2, 693–705, doi: 10.1093/gji/ggx158.

Vallée, M., and M. Bouchon (2004). Imaging coseismic rupture in far field by slip patches, *Geophys. J. Int.* **156,** no. 3, 615–630.

Waldhauser, F., and D. P. Schaff (2008). Large-scale relocation of two decades of northern California seismicity using cross-correlation and double-difference methods, *J. Geophys. Res.* **113,** no. B8, doi: 10.1029/2007JB005479.

Wetzler, N., T. Lay, E. E. Brodsky, and H. Kanamori (2018). Systematic deficiency of aftershocks in areas of high coseismic slip for large subduction zone earthquakes, *Sci. Adv.* **4,** no. 2, doi: 10.1126/sciadv.aao3225.

Sergio Ruiz[1]
Jean-Baptiste Ammirati[1]
Leoncio Cabrera
Bertrand Potin
Department of Geophysics
Universidad de Chile
Blanco Encalada 2002
Santiago, Chile
sruiz@uchile.cl
jbaptiste@ing.uchile.cl
leonciocabrerac@gmail.com
bpotin@dgf.uchile.cl

Felipe Leyton
National Seismological Center
Universidad de Chile
Blanco Encalada 2002
Santiago, Chile
leyton@csn.uchile.cl

Raúl Madariaga[1]
Laboratoire de Geologie
PSL Université
Ecole Normale Supérieure and CNRS
24 rue Lhomond
75230 Paris Cedex 05
France
madariag@biotite.ens.fr

[1] Also at Seismic Risk Program, University of Chile, Santiago, Chile.